DOI: 10.19884/j.1672-5220.202404003

Mesoporous Ti_3C_2-Loaded Iron Phthalocyanine (FePc) Electrocatalyst for Efficient Oxygen Reduction Reaction under Alkaline Conditions

WANG Xin[1], HUI Mingming[1], YANG Shengyuan[1], BU Fanxing[2*], LUO Wei[1*]
1. College of Materials Science and Engineering, Donghua University, Shanghai 201620, China
2. Key Laboratory of Silicate Cultural Relics Conservation, Ministry of Education, Shanghai University, Shanghai 200444, China

Abstract: MXene has attracted great attention due to its high conductivity, large specific surface area and tunable surface functional groups. However, MXene (e.g., Ti_3C_2) nanosheets tend to stack and mainly offer in-plane sites, showing limited capability in improving the oxygen reduction reaction (ORR) performance of iron phthalocyanine (FePc). In this study, mesoporous Ti_3C_2 (Meso-Ti_3C_2) loaded FePc (FePc/Meso-Ti_3C_2) catalysts were prepared by a simple ultrasonic liquid-phase compounding strategy. Meso-Ti_3C_2 possesses abundant mesopores and edge sites, which optimize the coordination environment and the electronic structure of the FeN_4 center in FePc. This optimization improves the mass transfer and the accessibility of the active sites, synergistically enhancing the ORR performance of FePc. As a result, FePc/Meso-Ti_3C_2 shows excellent ORR activity and stability under alkaline conditions with a half-wave potential of 0.914 V against the reversible hydrogen electrode (RHE) and a Tafel slope of 57.2 mV/dec. Furthermore, the zinc-air battery assembled with FePc/Meso-Ti_3C_2 delivers a peak power density of 183.1 mW/cm^2 and a good long-term discharge stability, exceeding those of FePc/Ti_3C_2 and commercial 20% Pt/C catalysts (20% Pt by mass).

Keywords: mesoporous Ti_3C_2; iron phthalocyanine (FePc); oxygen reduction reaction; edge site
CLC number: O611 **Document code**: A
Article ID: 1672-5220(2025)03-0219-11

Open Science Identity (OSID)

0 Introduction

The oxygen reduction reaction (ORR) is crucial in electrochemical energy conversion and storage technologies, e.g., fuel cells[1] and metal-air batteries[2-3]. However, the ORR process involves the transfer of four electrons with the cleavage of the O—O bond and the maximum release of the energy and thus exhibits slow reaction kinetics, necessitating the use of suitable catalysts to enhance the reaction activity[4]. Despite the high ORR activity of noble metal-based catalysts, e.g., platinum (Pt)[5], their large-scale application is severely hindered by high cost, scarce reserves, and limited long-term durability[6]. Therefore, great efforts have been put into the design of low-cost, high-activity and stable non-noble metal-based ORR catalysts[7]. Among the reported non-noble metal-based ORR catalysts, iron phthalocyanine (FePc) catalysts have attracted extensive attention due to their unique FeN_4 active sites and low energy barriers during the ORR process[8-9]. However, FePc not only suffers from poor conductivity[10] and a strong propensity to aggregate, but also exhibits a two-dimensional planar symmetric structure and electron distribution at the FeN_4 active sites that is detrimental to the adsorption and activation of O_2. Loading them on conductive supports holds great potential in synergistically overcoming the above issues, and thus has been considered as one promising strategy to improve the ORR performance of FePc catalysts.

Currently, a variety of materials, including carbon nanotubes[11-12], metal hydroxides[13], metal sulfides[14], graphene[15-16] and MXene[17-18], have been utilized as supports for FePc. In particular, MXene has garnered widespread attention due to its outstanding conductivity, high specific surface area, adjustable compositions and surface functional groups[19]. For instance, the MXene-supported FePc catalyst developed by Li et al.[20] not only facilitated the dispersion of FePc, but also reduced the local charge density of FeN_4, elevated the spin state of iron, improved the adsorption and activation of O_2, and thus enhanced its ORR performance. Dai et al.[21] further designed an alkalized MXene-supported FePc catalyst. The oxygen-containing functional groups on the MXene surface induce changes in the coordination environment of the FeN_4 sites, which reduces the number of unpaired electrons in the dz^2, dxz and dyz orbitals and causes the appropriate adsorption energy between the Fe center and

Received date: 2024-04-03
Foundation item: National Outstanding Youth Science Foundation, China (No. 52225204)
* Correspondence should be addressed to LUO Wei, email: wluo@dhu.edu.cn; BU Fanxing, email: fxbu@shu.edu.cn
Citation: WANG X, HUI M M, YANG S Y, et al. Mesoporous Ti_3C_2-loaded iron phthalocyanine (FePc) electrocatalyst for efficient oxygen reduction reaction under alkaline conditions [J]. *Journal of Donghua University (English Edition)*, 2025, 42(3): 219-229.

the ORR intermediates, thereby reinforcing the intrinsic reaction activity. However, MXene has a strong tendency to restack, which can obstruct ion transport and reduce the accessibility of active sites[22]. Recently, two-dimensional porous nanosheets have garnered substantial interest due to their abundant in-plane mesopores and edge sites[23-24]. This structure can not only address the previously mentioned challenges but also hold great potential in further optimizing the electronic structure of FeN_4 sites via edge effects. Employing mesoporous MXene, e. g., mesoporous Ti_3C_2 (Meso-Ti_3C_2), as a support for FePc is expected to markedly improve the ORR performance.

Therefore, we synthesized FePc/Meso-Ti_3C_2 electrocatalysts by using Meso-Ti_3C_2 to anchor the FePc molecules through a simple ultrasonic liquid-phase compounding strategy. The abundant edge unsaturated sites on Meso-Ti_3C_2 play a crucial role in optimizing the coordination environment and electronic structure of the FeN_4 center. Moreover, the Meso-Ti_3C_2 enhances mass transfer and active site accessibility, leading to a significant improvement in the ORR performance of FePc. The optimized FePc/Meso-Ti_3C_2 electrocatalyst exhibits superior ORR activity and stability compared to FePc/Ti_3C_2, featuring a half-wave potential of 0.914 V against the reversible hydrogen electrode (RHE), a Tafel slope of 57.2 mV/dec, and a turnover frequency of 2.79 s^{-1} at 0.90 V. Furthermore, the zinc-air battery assembled with the FePc/Meso-Ti_3C_2 catalyst achieved a peak power density of 183.1 mW/cm^2, superior to that of the commercial 20% Pt/C catalyst (20% Pt by mass).

1 Materials and Methods

1.1 Materials

Ti_3AlC_2 was purchased from Adamas Pharmaceuticals, Inc., USA. Lithium fluoride (LiF) and iron (II) phthalocyanine (FePc) were purchased from Aladdin Biochemical Technology Co., Ltd., China. Hydrofluoric acid (HF) and hydrochloric acid (HCl) were purchased from Shanghai Hushi Laboratorial Equipment Co., Ltd., China. Copper (II) sulfate ($CuSO_4$), dimethyl sulfoxide (DMSO) and *N*, *N*-dimethylformamide (DMF) were purchased from Sa'en Chemical Technology (Shanghai) Co., Ltd., China. Nafion was purchased from Sigma-Aldrich (Shanghai) Trading Co., Ltd., USA.

1.2 Synthesis of Ti_3C_2

Ti_3C_2 was synthesized via the modified minimally intensive layer delamination (MILD)[25] method. In brief, 8.0 g LiF was added to 100 mL HCl solution (9 mol/L), and the mixture was stirred for 10 min at room temperature. Subsequently, 5.0 g Ti_3AlC_2 was gradually added to the mixture over 30 min. The obtained Ti_3C_2 was then thoroughly rinsed with water to remove acids, metal ions and LiF residues. When the pH of the supernatant reached 7, the resultant Ti_3C_2 precipitate was dispersed in 50 mL DMSO and stirred for 12 h to increase the interlayer distance. Following this, the colloidal solution was centrifuged and washed twice with water. The expanded Ti_3C_2 was then dispersed in 200 mL water and subjected to ultrasound for 1 h in an argon atmosphere. This colloidal dispersion was centrifuged at 3 000 r/min for 1 h to remove aggregates. Finally, the obtained single-layer Ti_3C_2 dispersion was collected and stored at 4 ℃ for experimental use.

1.3 Preparation of Meso-Ti_3C_2

The Meso-Ti_3C_2 with uniformly distributed pores was fabricated by one high redox potential difference-driven oxidation and the following chemical etching strategy[25]. Typically, 6 mL Ti_3C_2 suspension at a mass concentration of 20 mg/mL was added to 124 mL deionized water and stirred for 30 min to achieve a uniform dispersion. Subsequently, 240 μL $CuSO_4$ solution (1 mol/L) and 120 μL H_2O_2 were introduced to the mixture, and the reaction proceeded for 1 h. The resultant Ti_3C_2/TiO_2 composite was collected by centrifugation, and washed three times with water, and then redispersed in 120 mL H_2O. Following this, 0.3 mL HF solution (HF mass fraction: 40%) was added to remove TiO_2, and the reaction was allowed to continue for 1 h. The final products were collected via centrifugation and sequentially washed three times each with water and ethanol.

1.4 Preparation of FePc/Ti_3C_2 and FePc/Meso-Ti_3C_2

First, 15 mg Meso-Ti_3C_2 and 15 mg FePc were dissolved in DMF, respectively, and after ultrasonication (SB-5200DT ultrasonic cleaning machine, 300 W, 40 kHz) for 2 h, two solutions were mixed. Then, the mixed solution was stirred under vacuum conditions for 12 h to ensure uniform loading of FePc on the Meso-Ti_3C_2 surface. Finally, three washes were performed by using DMF and ethanol, respectively. The FePc/Meso-Ti_3C_2 complex was collected by centrifugation, with 2 mL water added, and freeze-dried for 48 h. The final product was a dried powder sample named FePc/Meso-Ti_3C_2. The catalysts synthesized with FePc and Meso-Ti_3C_2 at mass ratios of 1∶2 and 1∶3 were labeled 1∶2-FePc/Meso-Ti_3C_2 and 1∶3-FePc/Meso-Ti_3C_2, respectively. The preparation of FePc/Ti_3C_2 was similar to the method above, except that Meso-Ti_3C_2 was replaced by Ti_3C_2. The catalysts synthesized with FePc and Ti_3C_2 at mass ratios of 1∶2 and 1∶3 were labeled 1∶2-FePc/Ti_3C_2 and 1∶3-FePc/Ti_3C_2, respectively.

1.5 Characterizations

The morphologies of catalysts were investigated by using a Regulus8230 scanning electron microscope (HITACHI, Japan). Transmission electron microscopy (TEM) images were taken on a JEOL 2100F microscope

(JEOL Ltd., Japan) operated at a voltage of 200 kV. X-ray diffraction (XRD) measurements were conducted with a Rigaku D/Max-2550 PC diffractometer (Rigaku Corporation, Japan). X-ray photoelectron spectroscopy (XPS) spectra were obtained by using an Escalab 250Xi electron spectrometer (Thermo Fisher Scientific, USA) equipped with Al Kα radiation. Nitrogen sorption isotherms were tested at 77 K with an Autosorb IQ analyzer (Quantachrome Instruments, USA). Before the measurements, the samples were degassed under vacuum at 180 ℃ for at least 6 h. The Brunauer-Emmett-Teller (BET) method was employed for the determination of the specific surface area of the catalysts and the Barrett-Joyner-Halenda (BJH) model was employed to analyze the pore size distribution and pore volume.

1.6 Electrochemical measurements

All electrochemical experiments were conducted using a standard three-electrode system at the Princeton Model636A electrochemistry workstation (AMETEK Scientific Instruments, USA). The working electrode was a rotating disk glass carbon electrode (GCE) with a disk diameter of 5 mm and a surface area of 19.6 mm^2. A Pt wire served as the counter electrode, and an Ag/AgCl electrode (saturated in 3.5 mol/L KCl) was used as the reference electrode. All potentials were calibrated to the RHE by using the Nernst equation in electrolyte solutions of 0.1 mol/L KOH and 0.5 mol/L H_2SO_4.

$$E_{RHE} = E_{Ag/AgCl} + 0.197 + 0.059 \times pH, \quad (1)$$

where E_{RHE} is the electrode potential against the RHE; $E_{Ag/AgCl}$ is the applied potential against the Ag/AgCl electrode.

To prepare the working electrode, a sample (5 mg) was dispersed in 975 μL ethanol and 25 μL Nafion solution, followed by 30 min of ultrasonic treatment to create a homogeneous catalyst ink. Subsequently, the prepared ink was drop-cast onto a GCE and allowed to dry naturally. The resulting catalyst loading was 0.3 mg/cm^2. Before the measurement, the electrolyte was purged with O_2 gas for 20 min. Cyclic voltammetry (CV) curves were analyzed at a scan rate of 50 mV/s. Linear sweep voltammetry (LSV) measurements were conducted by using a rotating disk electrode (RDE) within a potential range of 0.2 to 1.1 V (vs. RHE) at a scan rate of 10 mV/s and a rotation speed of 1 600 r/min.

1.7 Zinc-air battery tests

The performance of the zinc-air battery was evaluated in comparison to a commercial zinc-air battery. The air cathode consisted of hydrophilic carbon cloth with a catalyst loading of 1.0 mg/cm^2. A polished zinc plate served as the anode, and a mixed solution of 6.0 mol/L KOH and 0.2 mol/L $Zn(CH_3COO)_2$ was utilized as the electrolyte. The performance was tested by using a LAND-2001A system and Model636A workstation (Beijing Zhuangshi Technology Co., Ltd., China).

2 Results and Discussion

2.1 Structural and morphological analysis of FePc/Ti_3C_2 and FePc/Meso-Ti_3C_2

Figure 1 shows the scanning electron microscopy (SEM) images of FePc/Ti_3C_2 and FePc/Meso-Ti_3C_2 at different magnifications. After loading FePc, the obtained FePc/Ti_3C_2 and FePc/Meso-Ti_3C_2 still maintain the two-dimensional nanosheet structure with no obvious change in morphology.

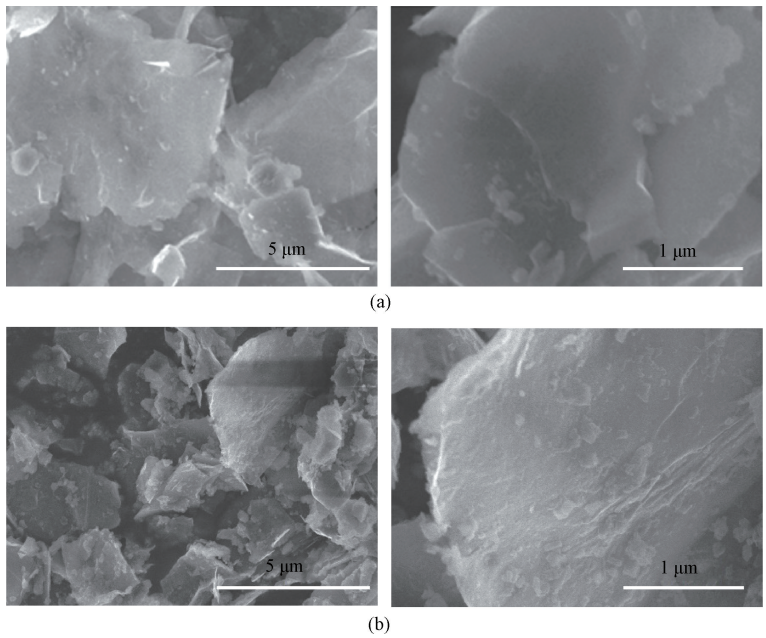

Fig. 1 SEM images of different samples at different magnifications: (a) FePc/Ti_3C_2; (b) FePc/Meso-Ti_3C_2

TEM images in Figs. 2(a)–2(c) illustrate that the Meso-Ti_3C_2 nanosheets exhibit a well-defined mesoporous structure with densely distributed in-plane mesopores throughout the two-dimensional structure. Upon FePc loading, the contrast in the TEM image of FePc/Meso-Ti_3C_2 noticeably increased (Fig. 2(d)), and small-sized FePc nanoparticles and clusters were observed on the surface of Meso-Ti_3C_2 (Fig. 2(e)). The high-resolution TEM image of FePc/Meso-Ti_3C_2 demonstrates that those nanoparticles possess one interlayer spacing of about 0.47 nm (Fig. 2(f)), corresponding to the (002) diffraction peak of FePc[26]. The energy dispersive X-ray spectroscopy (EDS) mapping results reveal a uniform distribution of C, O, N, Ti and Fe elements, indicating that FePc is evenly distributed throughout the whole FePc/Meso-Ti_3C_2 nanosheets (Fig. 2(g)).

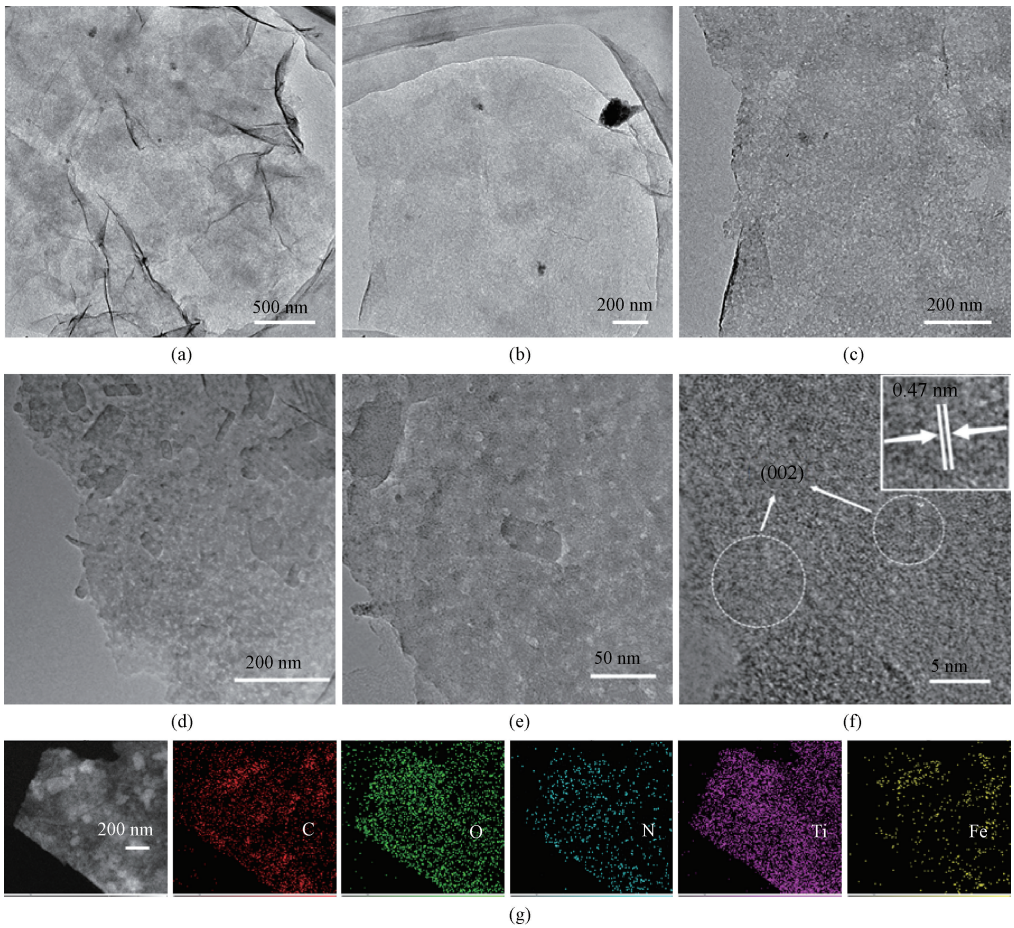

Fig. 2 Morphologies and element distribution of samples: (a)–(c) TEM images of Meso-Ti_3C_2; (d)–(f) TEM images of FePc/Meso-Ti_3C_2; (g) EDS elemental mapping of FePc/Meso-Ti_3C_2

Figure 3 shows the XRD patterns of FePc, FePc/Meso-Ti_3C_2 and FePc/Ti_3C_2. FePc shows two distinctive peaks at 2θ values of 6.71° and 26.06°, corresponding to its (002) and (011) crystal planes[17, 27], respectively. By contrast, the characteristic peaks of FePc are almost not viewed on the XRD patterns of FePc/Ti_3C_2 and FePc/Meso-Ti_3C_2, suggesting the uniform dispersion of FePc on the Ti_3C_2 and Meso-Ti_3C_2[28].

The nitrogen adsorption-desorption analysis results are summarized in Table 1. FePc/Meso-Ti_3C_2 shows a specific surface area of 111.4 m^2/g, representing an increase about 1.6-fold over that of FePc/Ti_3C_2, indicating more exposed sites. In addition, the total pore volume and average pore size of FePc/Meso-Ti_3C_2 are also higher than those of FePc/Ti_3C_2.

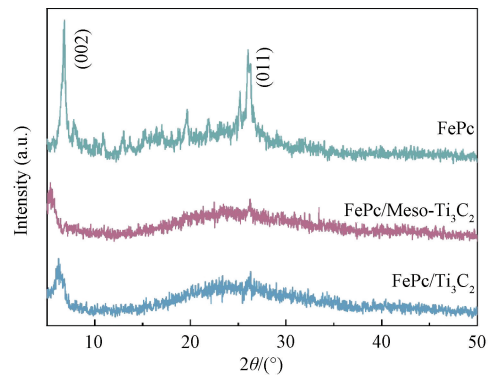

Fig. 3 XRD patterns of FePc, FePc/Meso-Ti_3C_2 and FePc/Ti_3C_2

Table 1 Specific surface area, total pore volume and average pore size of FePc/Ti_3C_2 and FePc/Meso-Ti_3C_2

Sample	Specific surface area/(m^2/g)	Total pore volume/(cm^3/g)	Average pore size/nm
FePc/Ti_3C_2	71.5	9.1	1.9
FePc/Meso-Ti_3C_2	111.4	22.1	4.2

Furthermore, the pore size distributions of both samples are compared in Fig. 4, where dV/dD represents the rate of change of pore volume per unit change in pore diameter. FePc/Meso-Ti_3C_2 features a concentrated pore size at approximately 3.8 nm, which is larger than that of FePc/Ti_3C_2 (1.8 nm). The larger pore size can help to promote the mass transfer and improve the active site accessibility[29].

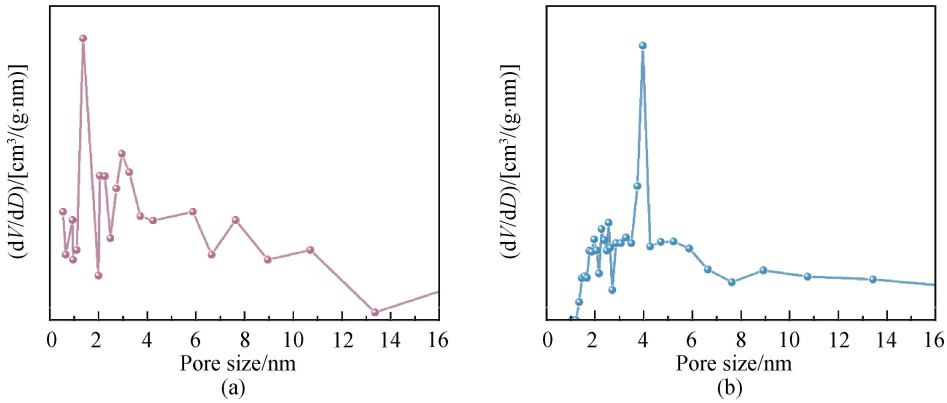

Fig. 4 Pore size distribution curves: (a) FePc/Ti_3C_2; (b) FePc/Meso-Ti_3C_2

XPS spectra of FePc/Ti_3C_2 and FePc/Meso-Ti_3C_2 are shown in Fig. 5. Despite the weak XPS signal, FePc/Meso-Ti_3C_2 demonstrates a discernible Fe 2p peak shift toward higher binding energies compared to FePc/Ti_3C_2 (Figs. 5(a) and 5(b)).

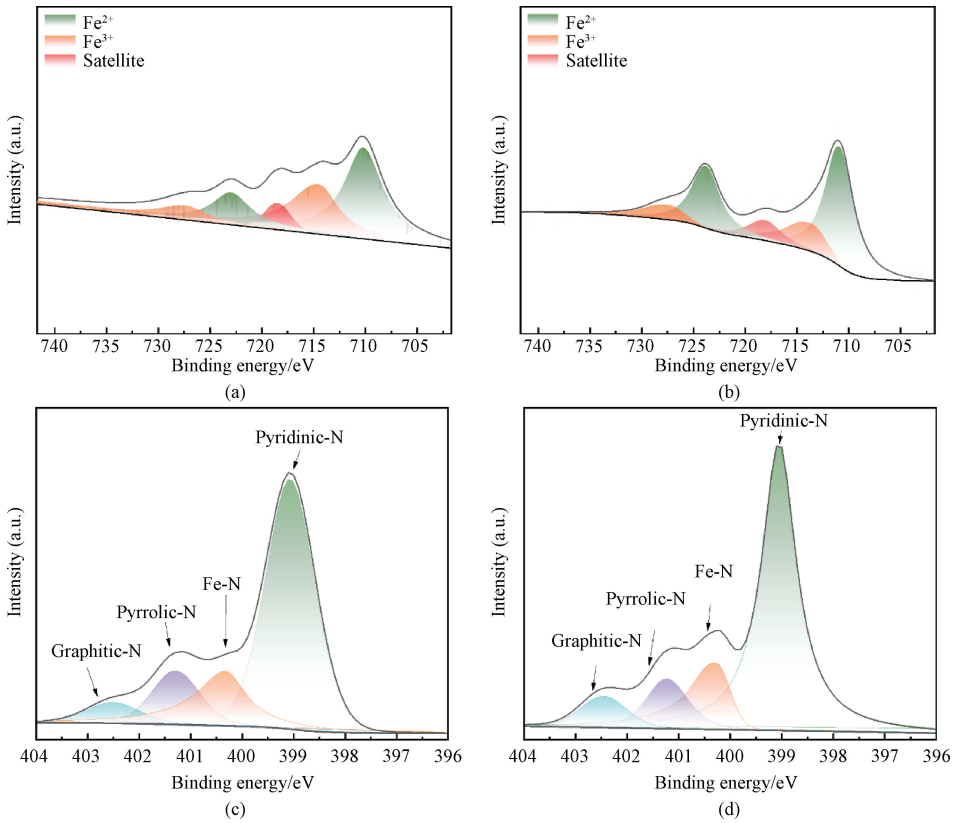

Fig. 5 XPS spectra of samples: (a) Fe 2p of FePc/Ti_3C_2; (b) Fe 2p of FePc/Meso-Ti_3C_2; (c) N 1s of FePc/Ti_3C_2; (d) N 1s of FePc/Meso-Ti_3C_2

Specifically, the Fe^{2+} signal peaks occur at 710.1 eV and 723.0 eV[30] for FePc/Ti_3C_2, while they increase to 711.0 eV and 723.9 eV for FePc/Meso-Ti_3C_2. Similarly, the Fe^{3+} signal peaks for FePc/Ti_3C_2 are located at 714.4 eV and 727.6 eV, and they shift to 714.5 eV and 727.8 eV for FePc/Meso-Ti_3C_2. The higher binding energies mean a stronger electronic interaction between Meso-Ti_3C_2 and FeN_4 structural sites, and imply more stable coordination of Fe atoms in FePc/Meso-Ti_3C_2, which can reduce the local electron density at the Fe atoms center[31].

Figures 5(c) and 5(d) display the N 1s high-resolution XPS spectra of FePc/Ti_3C_2 and FePc/Meso-Ti_3C_2, both of which can be fitted into four signal peaks: pyridinic-N, Fe-N, pyrrolic-N and graphitic-N[32]. Fe-N is identified as the active site for ORR in alkaline electrolytes. In comparison to FePc/Ti_3C_2, the Fe-N peak of FePc/Meso-Ti_3C_2 exhibits a shift of 0.2 eV, indicative of enhanced electron transfer. This result shows that Meso-Ti_3C_2 can further optimize the coordination environment and electronic structure of FePc, as compared to Ti_3C_2.

2.2 Electrochemical ORR performance

Subsequently, we assessed the ORR performance of FePc/Ti_3C_2 and FePc/Meso-Ti_3C_2 at different FePc loadings. The commercial 20% Pt/C catalyst (20% Pt by mass), designated as 20% Pt/C, was examined as a reference. All experiments were performed in an oxygen-saturated 0.1 mol/L KOH electrolyte solution.

The ORR polarization curves obtained from LSV in Fig. 6 reveal that the half-wave potential $E_{1/2}$ for FePc/Meso-Ti_3C_2 is 0.914 V vs. RHE. Similarly, $E_{1/2}$ for FePc/Ti_3C_2 is 0.895 V vs. RHE. For both catalysts, the ORR performance is progressively enhanced with an increase in FePc loading. This indicates that escalating FePc amounts produces more interfaces between FePc and substrates, and more active sites, thus augmenting the ORR performance. Obviously, FePc/Meso-Ti_3C_2 demonstrates the highest half-wave potential which is superior to that of FePc/Ti_3C_2, 20% Pt/C and the reported non-noble metal-based ORR catalysts (Table 2), suggesting that mesopore engineering of Ti_3C_2 can further enhance the ORR performance of FePc.

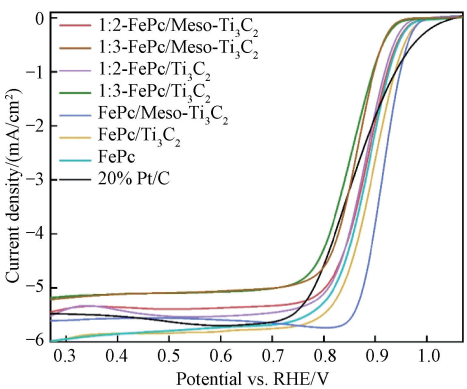

Fig. 6 ORR polarization curves of catalysts measured in 0.1 mol/L KOH solution at 1 600 r/min

Table 2 Comparison of ORR performance in 0.1 mol/L KOH for FePc/Meso-Ti_3C_2 and the reported non-noble metal-based ORR catalysts

Catalyst	$E_{1/2}$ vs. RHE/V	j_k/(mA/cm^2)	Ref.
Fe-CSA@NC	0.90	5.61	[33]
FeMn/MnN_4C	0.90	7.71	[34]
Fe/NC-3	0.90	4.00	[35]
Fe-N-C/MXene	0.84	—	[36]
Fe/Co@NCWO_2-x	0.87	—	[37]
FeSA/FeONC/NSC	0.86	32.15	[38]
Fe_2N_6	0.912	19.40	[39]
Fe_2S_2@CN	0.89	—	[40]
FeH-N-C	0.91	7.00	[41]
H-3DOM-Co/ONC	0.841	5.03	[4]
A-MnO_2/NSPC	0.87	42.79	[42]
FeN_4-Te_n	0.867	—	[43]
FePc/Meso-Ti_3C_2	0.914	11.33	**This work**

To better understand the ORR performance of FePc/Meso-Ti_3C_2, a series of characterizations were carried out. Figure 7 illustrates the kinetic current density j_k of FePc/Meso-Ti_3C_2, FePc/Ti_3C_2, FePc and 20% Pt/C at potentials of 0.85 V and 0.90 V. At 0.85 V, FePc/Meso-Ti_3C_2 achieves a j_k of 185.90 mA/cm^2, which is about nine times that of FePc/Ti_3C_2. At 0.90 V, the j_k values for FePc/Meso-Ti_3C_2, FePc/Ti_3C_2, FePc and 20% Pt/C are calculated as 11.33, 4.73, 3.39 and 2.59 mA/cm^2, respectively. The j_k of FePc/Meso-Ti_3C_2 is the highest, which reveals that the introduction of in-plane mesopores in Ti_3C_2 facilitates electron transfer.

Figures 8(a) and 8(b) depict the Tafel plots of the catalysts. The Tafel slope of FePc/Meso-Ti_3C_2 is 57.2 mV/dec, which is lower than that of other catalysts. The lowest value indicates that the FePc/Meso-Ti_3C_2 possesses the fastest kinetics. To assess the intrinsic ORR activity of the FePc/Meso-Ti_3C_2, turnover frequency (TOF) curves are plotted in Fig. 8(c). The TOF value of FePc/Meso-Ti_3C_2 at 0.90 V is 2.79 s^{-1}, representing about 1.75 times that of FePc/Ti_3C_2 (1.59 s^{-1}). The enhanced activity of FePc/Meso-Ti_3C_2 can be attributed to the more effective modulation of the coordination environment and the electronic structure of FePc by the edge sites of Meso-Ti_3C_2. Figure 8(d) showcases the Nyquist plots of FePc/Meso-Ti_3C_2, FePc/Ti_3C_2 and FePc. The charge transfer resistance of FePc/Meso-Ti_3C_2 is lower than that of FePc/Ti_3C_2, further

verifying its better reaction kinetics. According to the above results, the excellent ORR performance of FePc/Meso-Ti_3C_2 can be attributed to the following several points. First, the substrate can disperse FePc to promote the full exposure of active sites. Second, the edge sites can efficiently optimize the coordination environment and electronic structure of FePc to enhance its intrinsic ORR activity. The third but not the last, the mesoporous structure can promote the mass transfer and improve the active site accessibility.

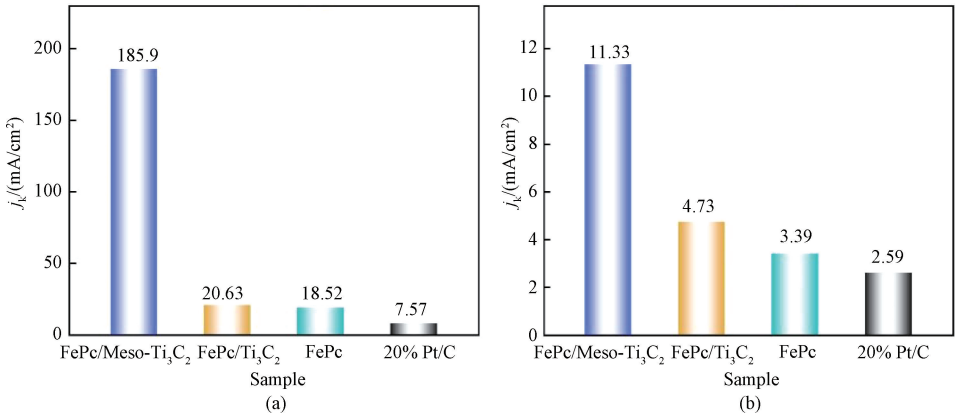

Fig. 7 Kinetic current density of FePc/Meso-Ti_3C_2, FePc/Ti_3C_2, FePc and 20% Pt/C at different potentials: (a) 0.85 V; (b) 0.90 V

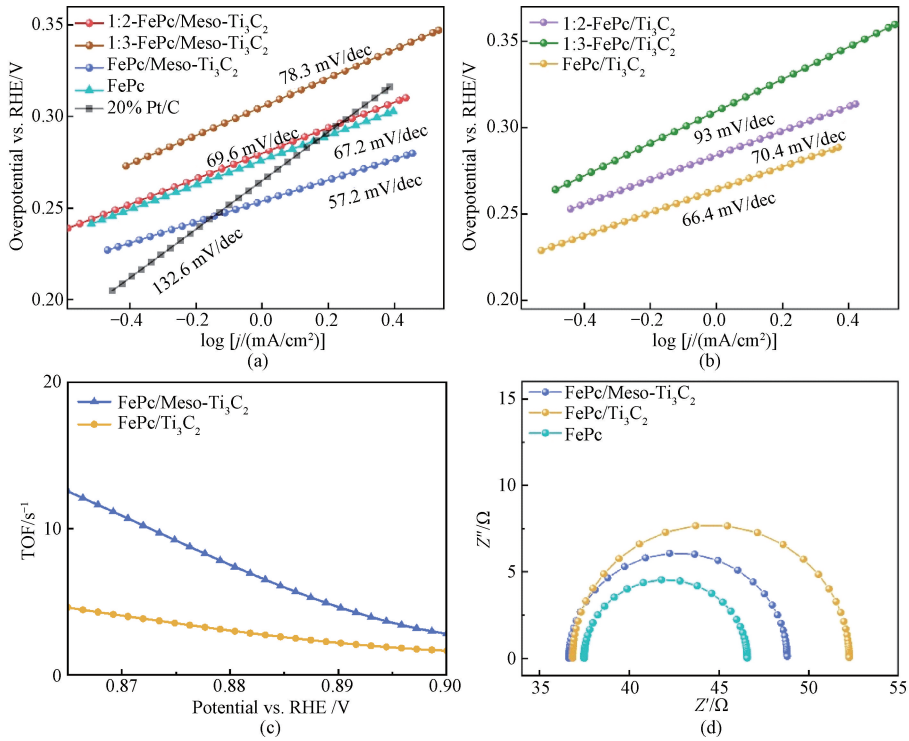

j—current density; Z'—real part of impedance; Z''—imaginary part of impedance.

Fig. 8 Electrochemical properties: (a) Tafel plots of FePc/Meso-Ti_3C_2 with different FePc loadings, FePc and 20% Pt/C; (b) Tafel plots of FePc/Ti_3C_2 with different FePc loadings; (c) TOF curves of FePc/Meso-Ti_3C_2 and FePc/Ti_3C_2; (d) Nyquist plots of FePc/Meso-Ti_3C_2, FePc/Ti_3C_2 and FePc in 0.1 mol/L KOH

To further evaluate the application potential, the electrochemical performance of a zinc-air battery assembled with the FePc/Meso-Ti_3C_2 catalyst was investigated. Figure 9(a) illustrates the polarization and corresponding power density curves for the FePc/Meso-Ti_3C_2, FePc/Ti_3C_2 and 20% Pt/C catalysts. The peak power density of FePc/Meso-Ti_3C_2 is 183.1 mW/cm^2, higher than that of FePc/Ti_3C_2 (153.2 mW/cm^2) and 20% Pt/C (118.7 mW/cm^2). Furthermore, the discharge curves of zinc-air batteries with those catalysts at different current densities are shown in Fig. 9(b). The FePc/Meso-Ti_3C_2 catalyst endows the zinc-air battery with higher voltages, especially at high current densities, compared to FePc/Ti_3C_2 and 20% Pt/C catalysts. Moreover, when the current density j is recovered to 10 mA/cm^2, the voltage can be returned to its original value. The higher peak power density, discharge voltage and excellent stability solidly confirm that FePc/Meso-Ti_3C_2 possesses superior ORR performance and presents considerable prospects in practical zinc-air batteries.

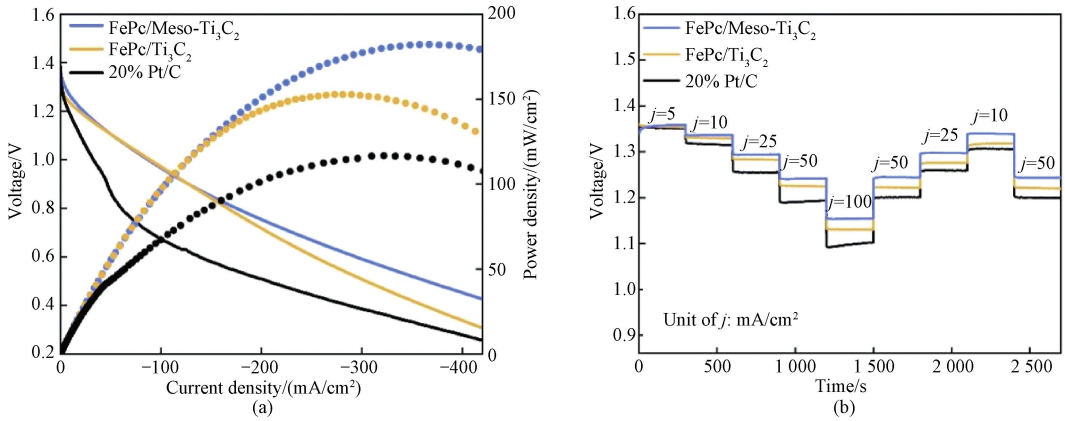

Fig. 9 Zinc-air battery performance: (a) polarization curves and corresponding power density curves of zinc-air batteries assembled with FePc/Meso-Ti_3C_2, FePc/Ti_3C_2 and 20% Pt/C catalysts; (b) discharge curves of zinc-air batteries assembled with FePc/Meso-Ti_3C_2, FePc/Ti_3C_2 and 20% Pt/C catalysts at different current densities

3 Conclusions

In summary, the FePc/Meso-Ti_3C_2 catalyst is synthesized by using a straightforward ultrasonic liquid-phase compounding strategy. Benefiting from the abundant in-plane mesopores and unsaturated edge sites in Meso-Ti_3C_2, the coordination environment and electronic structure of the FeN_4 center can be optimized to enhance its intrinsic activity. Furthermore, improvements in the mass transfer and the accessibility of active sites can accelerate the ORR kinetics, thereby synergistically improving the ORR performance of FePc. As a result, the FePc/Meso-Ti_3C_2 catalyst exhibits a high half-wave potential (0.914 V vs. RHE) and a low Tafel slope (57.2 mV/dec), outperforming both FePc/Ti_3C_2 and commercial 20% Pt/C catalysts. The zinc-air battery employing the FePc/Meso-Ti_3C_2 catalyst showcases an exceptional peak power density (183.1 mW/cm^2) and good cycling stability. This study not only introduces a highly catalytic active cathode ORR catalyst for zinc-air batteries, but also presents a novel mesopore engineering strategy to enhance the electrocatalytic performance of molecular catalysts.

References

[1] SHI L, LIU D, LIN X N, et al. Stable and high-performance flow H_2-O_2 fuel cells with coupled acidic oxygen reduction and alkaline hydrogen oxidation reactions[J]. *Advanced Materials*, 2024, 36(23): 2314077.

[2] LIU Y Y, ZHOU L M, LIU S L, et al. Fe, N-inducing interfacial electron redistribution in NiCo spinel on biomass-derived carbon for bi-functional oxygen conversion[J]. *Angewandte Chemie International Edition*, 2024, 63(16): e202319983.

[3] SUNTIVICH J, GASTEIGER H A, YABUUCHI N, et al. Design principles for oxygen-reduction activity on perovskite oxide catalysts for fuel cells and metal-air batteries[J]. *Nature Chemistry*, 2011, 3(7): 546-550.

[4] YAO W, HU A Q, DING J T, et al. Hierarchically ordered macro-mesoporous electrocatalyst with hydrophilic surface for efficient oxygen reduction reaction[J]. *Advanced Materials*, 2023, 35(30): 2301894.

[5] LIAN Y B, YANG W J, ZHANG C F, et al. Unpaired 3d electrons on atomically dispersed cobalt centres in coordination polymers regulate both oxygen reduction reaction (ORR) activity and selectivity for use in zinc-air batteries[J]. *Angewandte Chemie International Edition*, 2020, 59(1): 286-294.

[6] GE X M, SUMBOJA A, WUU D, et al.

Oxygen reduction in alkaline media: from mechanisms to recent advances of catalysts[J]. *ACS Catalysis*, 2015, 5(8): 4643-4667.
[7] MISTRY H, VARELA A S, KÜHL S, et al. Nanostructured electrocatalysts with tunable activity and selectivity[J]. *Nature Reviews Materials*, 2016, 1(4): 16009.
[8] ZHANG Z P, DOU M L, JI J, et al. Phthalocyanine tethered iron phthalocyanine on graphitized carbon black as superior electrocatalyst for oxygen reduction reaction[J]. *Nano Energy*, 2017, 34: 338-343.
[9] BAKER R, WILKINSON D P, ZHANG J J. Electrocatalytic activity and stability of substituted iron phthalocyanines towards oxygen reduction evaluated at different temperatures[J]. *Electrochimica Acta*, 2008, 53(23): 6906-6919.
[10] LUO Y J, CHEN Y H, XUE Y L, et al. Electronic structure regulation of iron phthalocyanine induced by anchoring on heteroatom-doping carbon sphere for efficient oxygen reduction reaction and Al-air battery[J]. *Small*, 2022, 18(2): 2105594.
[11] ZHU S, DING L T, ZHANG X H, et al. Biaxially-strained phthalocyanine at polyoxometalate@carbon nanotube heterostructure boosts oxygen reduction catalysis[J]. *Angewandte Chemie International Edition*, 2023, 62(42): e202309545.
[12] XU S X, DING Y X, DU J, et al. Immobilization of iron phthalocyanine on pyridine-functionalized carbon nanotubes for efficient nitrogen reduction reaction[J]. *ACS Catalysis*, 2022, 12(9): 5502-5509.
[13] LI G L, CAO S, LU Z F, et al. FePc nanoclusters modified NiCo layered double hydroxides in parallel with Ti_3C_2 MXene as a highly efficient and durable bifunctional oxygen electrocatalyst for zinc-air batteries[J]. *Applied Surface Science*, 2022, 591: 153142.
[14] LU Q, WU H, ZHENG X R, et al. Controllable constructing Janus homologous heterostructures of transition metal alloys/sulfides for efficient oxygen electrocatalysis[J]. *Advanced Energy Materials*, 2022, 12(42): 2202215.
[15] LI L B, TANG X N, HUANG S H, et al. Longitudinally grafting of graphene with iron phthalocyanine-based porous organic polymer to boost oxygen electroreduction[J]. *Angewandte Chemie International Edition*, 2023, 62(22): e202301642.
[16] LI J J, XIA W, TANG J, et al. Metal-organic framework-derived graphene mesh: a robust scaffold for highly exposed Fe-N_4 active sites toward an excellent oxygen reduction catalyst in acid media[J]. *Journal of the American Chemical Society*, 2022, 144(21): 9280-9291.
[17] TRAN P K L, TRAN D T, AUSTERIA P M, et al. Intermolecular metallic single-site complexes dispersed on $Mo_2TiC_2T_x/MoS_2$ heterostructure induce boosted solar-driven water splitting[J]. *Advanced Energy Materials*, 2023, 13(15): 2203844.
[18] ZHANG Y, ZHAO Q, DANIL B, et al. Oxygen-vacancy-induced formation of Pt-based intermetallics on MXene with strong metal-support interactions for efficient oxygen reduction reaction[J]. *Advanced Materials*, 2024, 36(25): 2400198.
[19] BAI X, GUAN J Q. MXenes for electrocatalysis applications: modification and hybridization[J]. *Chinese Journal of Catalysis*, 2022, 43(8): 2057-2090.
[20] LI Z L, ZHUANG Z C, LV F, et al. The marriage of the FeN_4 moiety and MXene boosts oxygen reduction catalysis: Fe 3d electron delocalization matters[J]. *Advanced Materials*, 2018, 30(43): 1803220.
[21] DAI Y K, LIU B, ZHANG Z Y, et al. Tailoring the d-orbital splitting manner of single atomic sites for enhanced oxygen reduction[J]. *Advanced Materials*, 2023, 35(14): 2210757.
[22] ZHANG G X, YANG H, ZHOU H J, et al. MXene-mediated interfacial growth of 2D-2D heterostructured nanomaterials as cathodes for Zn-based aqueous batteries[J]. *Angewandte Chemie International Edition*, 2024, 63(18): e202401903.
[23] SHI T L, HOU X, GUO S Q, et al. Nanohole-boosted electron transport between nanomaterials and bacteria as a concept for nano-bio interactions[J]. *Nature Communications*, 2021, 12(1): 493.
[24] XIE M, LUO W, QIU P P. Mesoporous carbon nanofibers loaded with ordered PtFe alloy nanoparticles for electrocatalytic nitrate reduction to ammonia[J]. *Journal of Donghua University (English Edition)*, 2024, 41(4): 365-376.
[25] BU F X, SUN Z H, ZHOU W H, et al. Reviving Zn^0 dendrites to electroactive Zn^{2+} by mesoporous MXene with active edge sites[J]. *Journal of the American Chemical Society*, 2023, 145(44): 24284-24293.
[26] ZHANG W, ZHANG J W, WANG N, et al. Two-electron redox chemistry via single-atom catalyst for reversible zinc-air batteries[J]. *Nature Sustainability*, 2024, 7: 463-473.
[27] ZHAO Q N, ZHOU W Z, ZHANG M X, et al. Edge-enriched $Mo_2TiC_2T_x/MoS_2$ heterostructure with coupling interface for selective NO_2 monitoring[J]. *Advanced Functional Materials*, 2022, 32(39): 2203528.
[28] BASOVA T V, KISELEV V G, DUBKOV I S,

et al. Optical spectroscopy and XRD study of molecular orientation, polymorphism, and phase transitions in fluorinated vanadyl phthalocyanine thin films[J]. *The Journal of Physical Chemistry C*, 2013, 117(14): 7097-7106.

[29] ZHANG Y, LIU Y Q, ZHOU J P, et al. Preparation of high conductive medium and establishment of large capacity conductive channel [J]. *Advanced Materials*, 2023, 35(47): 2307363.

[30] ZHANG J, ZHAO Y F, ZHAO W T, et al. Improving electrocatalytic oxygen evolution through local field distortion in Mg/Fe dual-site catalysts[J]. *Angewandte Chemie International Edition*, 2023, 62(52): e202314303.

[31] NGUYEN T H, TRAN P K L, DINH V A, et al. Metal single-site molecular complex-MXene heteroelectrocatalysts interspersed graphene nanonetwork for efficient dual-task of water splitting and metal-air batteries [J]. *Advanced Functional Materials*, 2023, 33(7): 2210101.

[32] PENG W, LIU J X, LIU X Q, et al. Facilitating two-electron oxygen reduction with pyrrolic nitrogen sites for electrochemical hydrogen peroxide production[J]. *Nature Communications*, 2023, 14(1): 4430.

[33] HUANG H J, YU D S, HU F, et al. Clusters induced electron redistribution to tune oxygen reduction activity of transition metal single-atom for metal-air batteries [J]. *Angewandte Chemie International Edition*, 2022, 61(12): e202116068.

[34] LIU H, JIANG L Z, KHAN J, et al. Decorating single-atomic Mn sites with FeMn clusters to boost oxygen reduction reaction[J]. *Angewandte Chemie International Edition*, 2023, 62(3): e202214988.

[35] LIU M J, LEE J, YANG T C, et al. Synergies of Fe single atoms and clusters on N-doped carbon electrocatalyst for pH-universal oxygen reduction[J]. *Small Methods*, 2021, 5(5): 2001165.

[36] JIANG L L, DUAN J J, ZHU J W, et al. Iron-cluster-directed synthesis of 2D/2D Fe-N-C/MXene superlattice-like heterostructure with enhanced oxygen reduction electrocatalysis[J]. *ACS Nano*, 2020, 14(2): 2436-2444.

[37] HAN Q L, ZHAO X M, LUO Y H, et al. Synergistic binary Fe-Co nanocluster supported on defective tungsten oxide as efficient oxygen reduction electrocatalyst in zinc-air battery [J]. *Advanced Science*, 2022, 9(4): 2104237.

[38] LEI Y, YANG F, XIE H M, et al. Biomass in situ conversion to Fe single atomic sites coupled with Fe_2O_3 clusters embedded in porous carbons for the oxygen reduction reaction [J]. *Journal of Materials Chemistry A*, 2020, 8(39): 20629-20636.

[39] LIU M, WANG X M, CAO S F, et al. Ferredoxin-inspired design of S-synergized Fe-Fe dual-metal center catalysts for enhanced electrocatalytic oxygen reduction reaction [J]. *Advanced Materials*, 2024, 36(19): 2309231.

[40] WANG M, ZHANG Z, ZHANG S L, et al. Non-planar nest-like [Fe_2S_2] cluster sites for efficient oxygen reduction catalysis [J]. *Angewandte Chemie International Edition*, 2023, 62(22): e202300826.

[41] TIAN H, SONG A L, ZHANG P, et al. High durability of Fe-N-C single-atom catalysts with carbon vacancies toward the oxygen reduction reaction in alkaline media [J]. *Advanced Materials*, 2023, 35(14): 2210714.

[42] HUO L P, LV M H, LI M J, et al. Amorphous MnO_2 lamellae encapsulated covalent triazine polymer-derived multi-heteroatoms-doped carbon for ORR/OER bifunctional electrocatalysis[J]. *Advanced Materials*, 2024, 36(18): 2312868.

[43] JI B F, GOU J L, ZHENG Y P, et al. Metalloid-cluster ligands enabling stable and active FeN_4-Te_n motifs for the oxygen reduction reaction [J]. *Advanced Materials*, 2022, 34(28): 2202714.

介孔 Ti_3C_2 负载酞菁铁电催化剂设计及其碱性条件下氧还原性能研究

王 鑫[1]，惠明明[1]，杨升元[1]，卜凡兴[2*]，罗 维[1*]

1. 东华大学 材料科学与工程学院，上海 201620
2. 上海大学 硅酸盐质文物保护教育部重点实验室，上海 200444

摘 要：MXene 因其高导电性、大比表面积和可调表面官能团而受到广泛关注。然而，MXene（如 Ti_3C_2）纳米片极易堆叠，其负载位点主要为面内位点，对酞菁铁（phthalocyanine，FePc）的氧还原性能提升有限。该文采用简单的超声液相复合策略制备了介孔 Ti_3C_2（Meso-Ti_3C_2）负载的 FePc 催化剂（FePc/Meso-Ti_3C_2）。Meso-Ti_3C_2 具有大量介孔和丰富的边缘位点，可优化 FePc 分子的四配位 FeN_4 中心的配位环境和电子结构，改善传质并提高活性位点的可及性，从而提升氧还原性能。FePc/Meso-Ti_3C_2 在碱性条件下展现出优异的氧还原反应活性和稳定性，半波电位为 0.914 V vs. RHE，Tafel 斜率为 57.2 mV/dec。以 FePc/Meso-Ti_3C_2 为催化剂的锌空气电池峰值功率密度为 183.1 mW/cm^2，且具有高循环稳定性，性能超过 FePc/Ti_3C_2 和商用 20% Pt/C 催化剂（Pt 质量占 20%）。

关键词：介孔 Ti_3C_2；酞菁铁；氧还原反应；边缘位点